

Sharp and window resonances in the 4*d* photoabsorption spectrum of Eu⁺ ions

X. M. Tong,^{1,*} D. Kato,¹ T. Watanabe,² and S. Ohtani^{1,2}

¹“Cold Trapped Ions” Project, ICORP, JST, Axis 3F, 1-40-2 Fuda Chofu, Tokyo 182-0024, Japan

² University of Electro-Communication, Chofu, Tokyo 182-0021, Japan

(Received 22 December 2000; published 20 August 2001)

We have studied the 4*d* photoabsorption process of Eu⁺ ions by the linear-density-response theory with the density-functional theory and an optimized effective potential and self-interaction correction. Different from the recent experimental observation, which found that the 4*d* photoabsorption spectrum of Eu⁺ ions is almost the same as that of neutral Eu atoms, our calculated 4*d* photoabsorption spectrum of Eu⁺ ions shows many sharp and window resonances, which do not appear in case of neutral Eu atoms. The discrepancies between the experimental observation and our calculation are due to the experimental energy resolution. The convoluted spectrum with the experimental energy resolution is in good agreement with the experimental observation. Moreover, we predict the 4*d* photoabsorption spectra with several given energy resolutions, which call for a further higher-resolution experiment.

DOI: 10.1103/PhysRevA.64.032716

PACS number(s): 32.80.Fb, 31.15.Ew

I. INTRODUCTION

The 4*d* giant resonance in photoionization process of rare gas has been interested in for a long time [1,2]. The broad resonance of the 4*d*-photoionization cross section for rare-gas atoms can be explained being due to the electron-electron dynamic correlation and the double-well potential for the final *f* partial wave [2,3]. Increasing the ionization degree, the evolution of the giant resonance is explained by “orbital collapse” of the *f* partial wave [2,4,5] and the resonance structure disappears for highly charged ions [6,7]. There are also many experimental studies [1,8–10] of the 4*d* photoionization cross sections for rare-earth atoms. The shape of giant resonance of rare-earth atoms is different from that of the rare-gas atoms due to the occupation of 4*f* electrons. The giant-resonance shape of Eu atoms is a typical example of the rare-earth atoms since the 4*f* orbit is half filled. Experiments [8,10] show that the width of giant resonance for Eu atoms is narrower than that of the rare-gas atoms and the line profile of the resonance is strongly asymmetric, similar to the Fano profile [11] of the autoionization state. Such features can be understood being due to a broad resonance of 4*d* spin-down electrons interaction with a sharp resonance (quasibound state) of 4*d* spin-up electrons [12] if we fill all the 4*f* electrons in the spin-up state. Recently, experiment [10] shows that the 4*d*-giant resonance spectrum of Eu⁺ ions is very similar to that of Eu atoms. Encouraged by our previous studies on Eu atoms [12], we have investigated the 4*d* photoabsorption spectrum of Eu⁺ ions. Surprisingly, we found a lot of sharp resonances as well as window resonances in the 4*d* photoabsorption spectrum. By convoluting our calculated results with the experimental energy resolution, our results are in good agreement with the experiment in Ref. [10]. Several convoluted spectra have been presented to call for further experimental studies. To investigate the mechanism of the sharp and window resonances, we have

decomposed different orbital contributions to the photoabsorption and identified that the very sharp resonance comes from 4*d*→*np* transition interaction with 5*p* to continuum transition, while the relative broad and window resonances come from 4*d*→*nf* transition interaction with 5*p* to continuum transition. Such interactions of a bound-bound transition with a bound-free transition result in a typical Fano profile [11]. Most of the calculated sharp and window resonances have been identified.

We will give a brief description of our theoretical method in Sec. II, and present our results and a discussion in Sec. III.

II. THEORETICAL METHOD

The theoretical method used in the present calculation is the same as in Ref. [12] with some modification in the numerical procedure to improve the numerical accuracy for the Green function near zero-energy region. For discussing convenience, we will repeat the theoretical method here with emphasis on the formulas we will use in the discussion.

The photoexcitation or photoionization cross sections from an initial state $|is\rangle$ to a final state $|js\rangle$ can be expressed as (atomic units $\hbar = m = e = 1$ are used throughout unless explicitly stated otherwise)

$$\sigma_{is}(\omega) = \frac{2\omega}{3} \frac{2\pi^2}{c} n_{is} \sum_{js} (1 - n_{js}) |\langle js | \mathbf{r} | is \rangle|^2 \times \delta(\omega - \epsilon_{js} + \epsilon_{is}), \quad (1)$$

where $|is\rangle$ and $|js\rangle$ are the solutions of the following one-electron Schrödinger-like equation

$$\left[-\frac{1}{2} \nabla^2 + V_s^{eff}(\mathbf{r}) \right] \phi_{is}(\mathbf{r}) = \epsilon_{is} \phi_{is}(\mathbf{r}). \quad (2)$$

Here $V_s^{eff}(\mathbf{r})$ is a spin-dependent effective potential and *s*, is the spin index (spin-up ↑ or spin-down ↓). For photoionization processes, the final states are unbound solutions of Eq. (2) with ϵ_{is} replaced by $\frac{1}{2}k^2$, where *k* is the photoelectron

*Email address: tong@hci.jst.go.jp

momentum and n_{i_s} and n_{j_s} are the occupation number of the initial and final states, respectively. Such an independent particle approximation (IPA) does not take the electron dynamic correlation into account and the calculated photoionization cross section near the giant resonance can not fully reproduce the experimental observations [13]. Meanwhile, the IPA model does not take into account the interaction between the photoexcitation and the photoionization from different shells, which results in the Fano profile. The electron dynamic correlation ignored in the IPA model can be taken into account by linear-density-response theory [13–17], which considers the effect of a weak time-dependent perturbation field on the electron density. The frequency-dependent induced density $\delta\rho(\mathbf{r},\omega)$ can be obtained by the Fourier transformation of the time-dependent field-induced density $\delta\rho(\mathbf{r},t)$:

$$\delta\rho(\mathbf{r},\omega) = \frac{1}{2\pi} \int_{-\infty}^{\infty} \delta\rho(\mathbf{r},t) e^{i\omega t} dt. \quad (3)$$

The induced density is related to an external field by the following relationship

$$\delta\rho(\mathbf{r},\omega) = \int \chi(\mathbf{r},\mathbf{r}',\omega) V^{ext}(\mathbf{r}',\omega) d^3\mathbf{r}', \quad (4)$$

where $\chi(\mathbf{r},\mathbf{r}',\omega)$ is the frequency-dependent susceptibility and

$$V^{ext}(\mathbf{r},\omega) = z, \quad (5)$$

is the dipole external field. The susceptibility can be determined by means of the first-order time-dependent perturbation theory [18] and expressed in terms of the eigenfunctions $\{\phi_{i_s}(\mathbf{r})\}$ and eigenvalues $\{\epsilon_{i_s}\}$ of the solutions of Eq. (2) as

$$\chi_s^{IPA}(\mathbf{r},\mathbf{r}',\omega) = \sum_{i_s,j_s} (n_{i_s} - n_{j_s}) \frac{\phi_{i_s}^*(\mathbf{r}) \phi_{j_s}(\mathbf{r}) \phi_{i_s}(\mathbf{r}') \phi_{j_s}^*(\mathbf{r}')}{\omega - (\epsilon_{j_s} - \epsilon_{i_s}) + i\eta}. \quad (6)$$

Here $i\eta$ is an imaginary infinitesimal used to ensure the outgoing wave boundary condition. Note that the η can also be treated as the experimental energy resolution with the Lorentzian line profile. The summation over i and j runs over all the bound and continuum states. Since the change of the electron density will result in a local field correction, the effective field or self-consistent field (SCF) $V_s^{SCF}(\mathbf{r},\omega)$ can be obtained by replacing Eq. (4) with

$$\begin{aligned} \delta\rho(\mathbf{r},\omega) &= \sum_s \int \chi_s^{IPA}(\mathbf{r},\mathbf{r}',\omega) V_s^{SCF}(\mathbf{r}',\omega) d^3\mathbf{r}' \\ &= \sum_s \delta\rho_s(\mathbf{r},\omega). \end{aligned} \quad (7)$$

We use the IPA potential obtained from the density-functional theory with an optimized effective potential and a self-interaction correction [19,20]. With such an IPA potential, $V_s^{SCF}(\mathbf{r},\omega)$ can be expressed as

$$\begin{aligned} V_s^{SCF}(\mathbf{r},\omega) &= V^{ext}(\mathbf{r},\omega) + \int \frac{\delta\rho(\mathbf{r}',\omega)}{|\mathbf{r}-\mathbf{r}'|} d^3\mathbf{r}' \\ &+ \left. \frac{\partial V_{xc}(\mathbf{r})}{\partial \rho_s(\mathbf{r})} \right|_{\rho_o(\mathbf{r})} \delta\rho_s(\mathbf{r},\omega). \end{aligned} \quad (8)$$

Here $\rho_o(\mathbf{r})$ is the ground-state electron density. The normal procedure is to solve Eqs. (7) and (8) iteratively until convergence is reached. However, an alternative and simpler procedure can be obtained by substituting Eq. (7) into Eq. (8) to get

$$\begin{aligned} \begin{bmatrix} V_{\uparrow}^{SCF}(\mathbf{r},\omega) \\ V_{\downarrow}^{SCF}(\mathbf{r},\omega) \end{bmatrix} &= \begin{bmatrix} V^{ext}(\mathbf{r},\omega) \\ V^{ext}(\mathbf{r},\omega) \end{bmatrix} + \int \begin{bmatrix} K_{\uparrow\uparrow}(\mathbf{r},\mathbf{r}') & K_{\uparrow\downarrow}(\mathbf{r},\mathbf{r}') \\ K_{\downarrow\uparrow}(\mathbf{r},\mathbf{r}') & K_{\downarrow\downarrow}(\mathbf{r},\mathbf{r}') \end{bmatrix} \\ &\times \begin{bmatrix} V_{\uparrow}^{SCF}(\mathbf{r}',\omega) \\ V_{\downarrow}^{SCF}(\mathbf{r}',\omega) \end{bmatrix} d^3\mathbf{r}', \end{aligned} \quad (9)$$

with

$$\begin{aligned} K_{\uparrow\uparrow}(\mathbf{r},\mathbf{r}') &= \int \frac{\chi_{\uparrow}^{IPA}(\mathbf{r}',\mathbf{r}'',\omega)}{|\mathbf{r}-\mathbf{r}''|} d^3\mathbf{r}'' \\ &+ \left. \frac{\partial V_{xc}(\mathbf{r})}{\partial \rho_{\uparrow}(\mathbf{r})} \right|_{\rho_o(\mathbf{r})} \chi_{\uparrow}^{IPA}(\mathbf{r},\mathbf{r}',\omega) \\ K_{\downarrow\downarrow}(\mathbf{r},\mathbf{r}') &= \int \frac{\chi_{\downarrow}^{IPA}(\mathbf{r}',\mathbf{r}'',\omega)}{|\mathbf{r}-\mathbf{r}''|} d^3\mathbf{r}'' \\ &+ \left. \frac{\partial V_{xc}(\mathbf{r})}{\partial \rho_{\downarrow}(\mathbf{r})} \right|_{\rho_o(\mathbf{r})} \chi_{\downarrow}^{IPA}(\mathbf{r},\mathbf{r}',\omega) \\ K_{\uparrow\downarrow}(\mathbf{r},\mathbf{r}') &= \int \frac{\chi_{\downarrow}^{IPA}(\mathbf{r}',\mathbf{r}'',\omega)}{|\mathbf{r}-\mathbf{r}''|} d^3\mathbf{r}'' \\ K_{\downarrow\uparrow}(\mathbf{r},\mathbf{r}') &= \int \frac{\chi_{\uparrow}^{IPA}(\mathbf{r}',\mathbf{r}'',\omega)}{|\mathbf{r}-\mathbf{r}''|} d^3\mathbf{r}'' \end{aligned} \quad (10)$$

The integral equation (9) can now be rewritten as a linear equation, from which $V_s^{SCF}(\mathbf{r},\omega)$ can be readily solved by discretion in the \mathbf{r} space. Substituting the results of $V_s^{SCF}(\mathbf{r},\omega)$ into Eq. (7), we obtain the induced density $\delta\rho(\mathbf{r},\omega)$. Finally, the cross section can be obtained by the well known relationship

$$\sigma(\omega) = \frac{4\pi\omega}{c} \text{Im}[\alpha(\omega)], \quad (11)$$

where $\alpha(\omega)$ is the dynamical polarizability given by

$$\begin{aligned} \alpha(\omega) &= - \sum_s \int \int V^{ext}(\mathbf{r},\omega) \chi_s^{IPA}(\mathbf{r},\mathbf{r}',\omega) \\ &\times V_s^{SCF}(\mathbf{r}',\omega) d^3\mathbf{r} d^3\mathbf{r}'. \end{aligned} \quad (12)$$

The key issue here is how to calculate the susceptibility based on the IPA potential. Since the susceptibility can be written as a summation over all the orbits, we can calcu-

late the contributions of the susceptibility by the Green's function method as discussed in Ref. [13]. First we rewrite Eq. (6) as

$$\begin{aligned}
 \chi_s^{IPA}(\mathbf{r}, \mathbf{r}', \omega) &= \sum_{is, js} n_{is} \frac{\phi_{is}^*(\mathbf{r}) \phi_{js}(\mathbf{r}) \phi_{is}(\mathbf{r}') \phi_{js}^*(\mathbf{r}')}{\omega - (\varepsilon_{js} - \varepsilon_{is}) + i\eta} - \sum_{is, js} n_{js} \frac{\phi_{is}^*(\mathbf{r}) \phi_{js}(\mathbf{r}) \phi_{is}(\mathbf{r}') \phi_{js}^*(\mathbf{r}')}{\omega - (\varepsilon_{js} - \varepsilon_{is}) + i\eta} \\
 &= \sum_{is} n_{is} \phi_{is}^*(\mathbf{r}) \phi_{is}(\mathbf{r}') \sum_{js} \frac{\phi_{js}(\mathbf{r}) \phi_{js}^*(\mathbf{r}')}{\omega - (\varepsilon_{js} - \varepsilon_{is}) + i\eta} + \sum_{is} n_{is} \phi_{is}(\mathbf{r}) \phi_{is}^*(\mathbf{r}') \sum_{js} \frac{\phi_{js}^*(\mathbf{r}) \phi_{js}(\mathbf{r}')}{\omega - (\varepsilon_{js} - \varepsilon_{is}) - i\eta} \\
 &\equiv \sum_{is} n_{is} \phi_{is}^*(\mathbf{r}) \phi_{is}(\mathbf{r}') G(\mathbf{r}, \mathbf{r}'; \omega + \varepsilon_{is} + i\eta) + \sum_{is} n_{is} \phi_{is}(\mathbf{r}) \phi_{is}^*(\mathbf{r}') G^*(\mathbf{r}, \mathbf{r}'; \varepsilon_{is} - \omega + i\eta) \quad (13)
 \end{aligned}$$

and then calculate the Green's function exactly the same way as in Ref. [12]. With the calculated Green's functions, we can construct the susceptibility from Eq. (13). Once the susceptibility is determined, $V_s^{SCF}(\mathbf{r}, \omega)$ is obtained by the solution of Eq. (9) and the cross section can be calculated by Eqs. (11) and (12). The linear-response method is usually referred to as a time-dependent technique. If we use V^{ext} instead of $V_s^{SCF}(\mathbf{r}, \omega)$ in Eq. (12), we reproduce the cross-section expression for the independent particle approximation. The independent particle approximation Eq. (1) will be referred to as the time-independent method since it does not take into account the time-dependent field-induced density correction.

The improvement of present method over the previous linear-density-response theory with the density-functional method [13] is that we use optimized effective potential in Eq. (2). Such optimized effective potential has taken into account the self-interaction correction [19]. With the optimized effective potential, we can describe the photoionization process better than the previous method.

III. RESULTS AND DISCUSSION

Based on the linear-density-response method, we can calculate the photoabsorption (photoexcitation and photoionization) cross section. Moreover, we can investigate the mechanism of abnormal behaviors, namely, the giant resonance in the photoionization process by decomposing each orbital contribution in Eq. (13) by including or excluding the orbital. Figure 1 shows our calculated photoabsorption cross sections of Eu atoms and Eu^+ ions around the 4d ionization threshold. (Note that we assume that all the seven 4f electrons are filled in the spin-up state.) For comparison, Fig. 2 shows the corresponding experimental spectra of Eu atoms [8] and Eu^+ ions [10]. Figure 1(a) shows that there are two groups of shape peaks ($4d \rightarrow np, nf$), which correspond to the two 4d ionization limits (spin-up and spin-down), locate in the lower energy side of the giant resonance for Eu atoms. As removing one outer shell (6s) electron, the 4d ionization threshold increases and the two groups of the bound-bound transition move into the giant resonance region for Eu^+ ions as shown in Fig. 1(b) while the experimental spectra of Eu atoms and

Eu^+ ions (as shown in Fig. 2) are very close to each other. Our calculation seems contradiction with the experimental observations [8,10] as shown in Fig. 2. In the experiment of Eu^+ ions the energy resolution ($E/\Delta E$) is improved from 130 to 350, only a tiny difference near the giant resonance peak is observed. Is the high experimental energy resolution good enough to observe the sharp and window resonances predicted in our calculations? To compare with the experimental spectra, we can; (1) convolute our calculated spectra with the experimental energy resolution and the energy resolution profile, namely, Gaussian or Lorentzian line profiles; (2) calculate the spectra directly with η in Eq. (6) as the energy resolution, which corresponds to Lorentzian profile. The equivalent of (1) and (2) has been checked in our calcu-

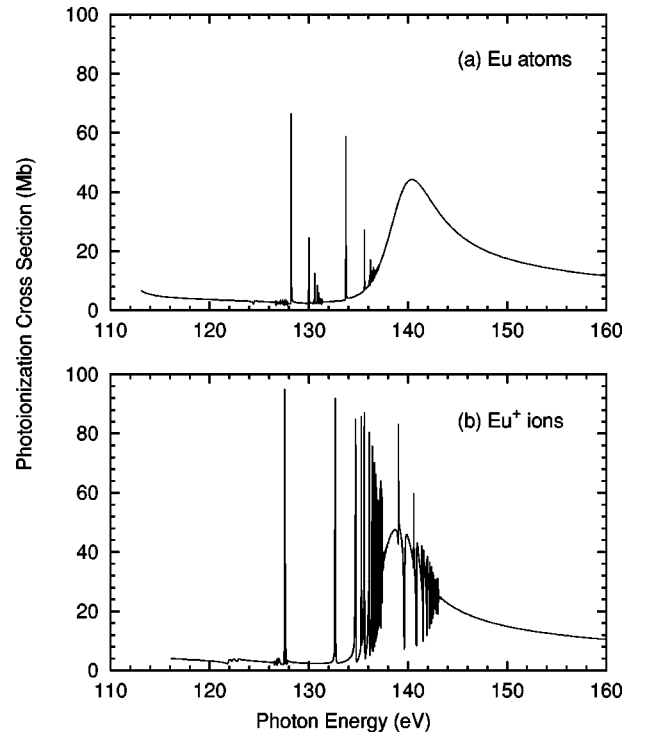


FIG. 1. The calculated 4d photoabsorption cross sections for (a) Eu atoms and (b) Eu^+ ions.

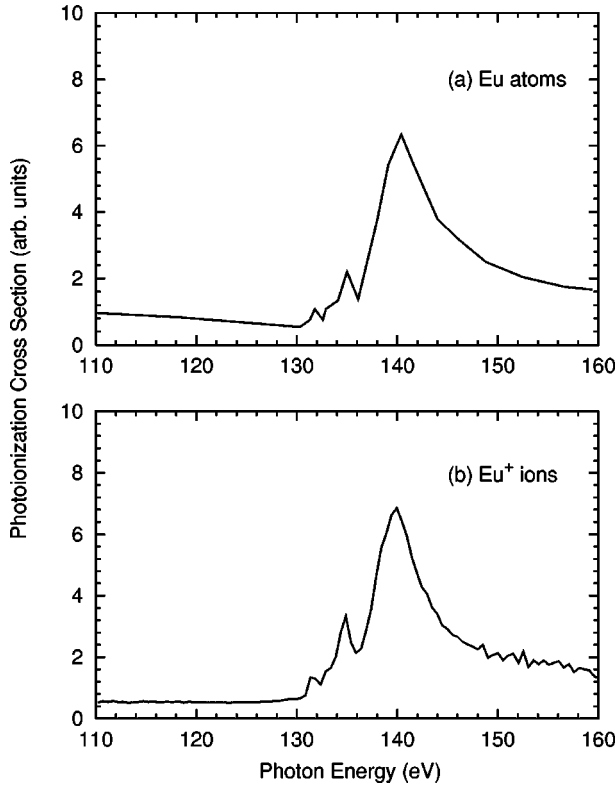


FIG. 2. The experimental $4d$ photoionization spectra for (a) Eu atoms [8] and (b) Eu^+ ions [10].

lations. Note that the advantages of scheme (2) are, (a) we can consider the experimental energy resolution directly in the calculation; (b) we can use relative large energy step in the calculation without losing sharp peak contributions. Figure 3 shows the convoluted spectra with different energy resolution τ (half-width at half-magnitude HWHM) for Eu atoms and Eu^+ ions. It shows that the $4d$ giant resonance spectrum of Eu atoms does not strongly depend on the τ , except for a few sharp resonances in the lower energy side of the giant resonance. For Eu^+ ions, the $4d$ giant resonance spectrum strongly depends on the τ . For lower energy resolution ($\tau=300$ meV), our calculated spectrum is in good agreement with the experiment one [10]. With increasing the energy resolution from $\tau=300$ meV to $\tau=200$ meV or even to $\tau=100$ meV, the pattern of the giant resonance of Eu^+ ions does not change dramatically, but more sharp resonance appears in the lower energy side of the giant resonance and more clearly peak splitting appears on the top of the giant resonance. With better energy resolution ($\tau=50$ meV), clear window resonances can be observed, but no accompany sharp resonance appears as shown in Fig. 1(b).

It is very interesting to compare the $4d$ photoabsorption of Eu atoms and Eu^+ ions with the $4d$ photoabsorption Xe-like isoelectronic sequence [5]. In both cases, from neutral atom to charged ions, bound-bound transitions become more pronounced in the spectra as they move closer to the peak of the $4d$ giant resonance. To study the detailed mechanisms of the $4d$ giant resonance of Eu^+ ions, we will decompose each individual orbital contributions in the following discussions.

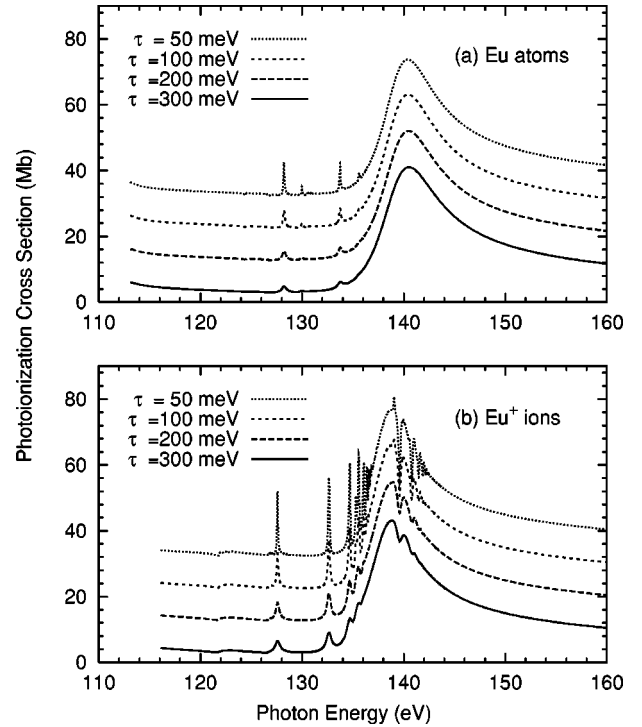


FIG. 3. The convoluted $4d$ photoabsorption spectra for (a) Eu atoms and (b) Eu^+ ions. The HWHM used in the convolution are 50 meV (dotted line), 100 meV (dashed line), 200 meV (long dashed line) and 300 meV (solid line), respectively with Lorentzian profile. The photoabsorption spectra are offset by 10, 20, 30 Mb, respectively, for clearly comparison.

Figure 4 shows the photoabsorption cross section for spin-up or spin-down states, which means that we set the susceptibility of spin-down or spin-up as zero in Eq. (6). Note that we assign the half-filled $4f$ electrons in the spin-up orbital. Meanwhile, for given bound state is with partial wave l in Eq. (13), the partial wave of the Green function should be $l \pm 1$ due to the dipole selection rule. In the calculation, we can include both $l \pm 1$ ($f+p$) or include only $l + 1$ (f only). Overall, we can see that two resonance groups from 130 to 137 and 138 to 143 eV are due to the $4d$ spin-down and $4d$ spin-up orbitals to the excited states. For the spin-up case, the transition to nf forms window resonance while the transition to np forms sharp resonance. The detailed interactions between the p state and f state also influence the pattern of the spectra as shown in Fig. 4(a). Different from the spin-up case, the transitions for the spin-down state to both nf or np states form resonance peaks. The width for the transition to np is much narrower than that to nf . All these imply that the interaction of nf with the continuum is stronger than that of np with the continuum. In Fig. 4(a), we see that the broad resonance (dashed curve) moves to the lower energy part (solid curve), while the position of window resonances does not change when we take into account the transition to the p partial wave. In Fig. 4, we clearly see that the $4d \rightarrow np, nf$ transitions for the spin-up state locate into the $4d$ photoionization region for the spin-down state. If we compare the $4d$ photoabsorption of the spin-up or spin-down state for Eu atoms and Eu^+ ions, the

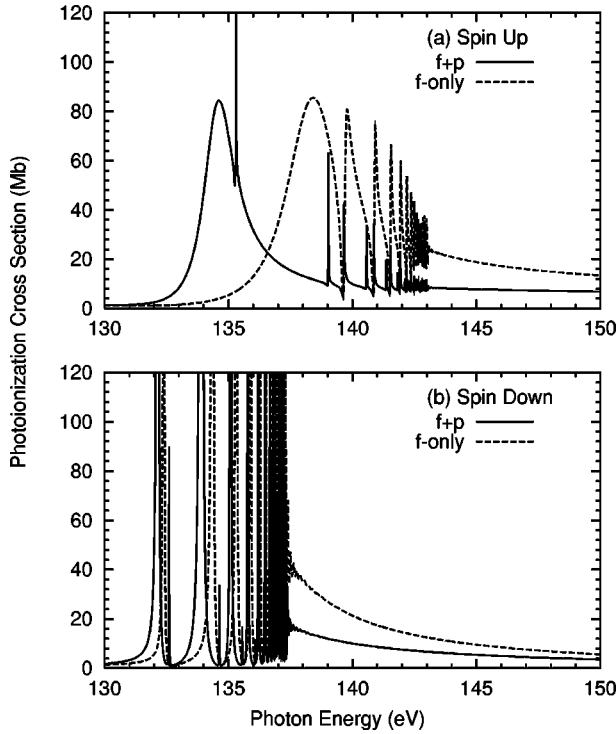


FIG. 4. The $4d$ photoabsorption spectra of Eu^+ ions for (a) spin-up electrons and (b) spin-down electrons. The solid line ($f+p$) means the transition to both $l \pm 1$ partial waves and the dashed line (f only) means the transition only to $l+1$ partial wave.

giant resonance moves close to the bound-bound transitions, similar to the $4d$ photoionization in the Xe-like isoelectronic sequence [5]. Due to the interaction between the transition in the $4d$ spin-up state and the $4d$ spin-down states, the Fano-profile resonance is formed in the giant resonance region. Therefore, the physical mechanism is similar to that of giant resonance in the Eu atom [12].

Now, we will ask whether the occupied $5p$ orbital plays an important role or not. Figure 5 shows the calculated photoabsorption spectra with $5p$ orbital or without $5p$ orbital in Eq. (13). Comparing Figs. 5(a) and 5(b), we see that the spectral pattern, especially the window resonance, changes dramatically without $5p$ orbital. Without $5p$ orbital, $4d \rightarrow nf$ transitions show sharp resonance pattern as shown in Fig. 5(b). So, we can conclude that the window resonance is due to $4d \rightarrow nf$ bound transition interaction with $5p$ to continuum transition, which results in a typically Fano profile.

Based on the above discussion, we can also assign the calculated spectra of Eu atoms and Eu^+ ions as we did for the Xe-like isoelectronic sequence. Figure 6 shows the assignment of the calculated spectra for (a) Eu atoms and (b) Eu^+ ions. Here we label the transition from $4d$ spin-up state as np or nf and the transition from $4d$ spin-down state as np' and nf' . In Fig. 6(a), we see that there is no nf state observed in Eu atoms since all the nf states are located in the outer potential well [12]. The strength of the transition to np state decreases as the principle quantum number n increases. In Fig. 6(b), we see that the transition to nf states has been observed in Eu^+ ions. Different from the transition to np state of Eu atoms, the transition strength to the nf' reaches

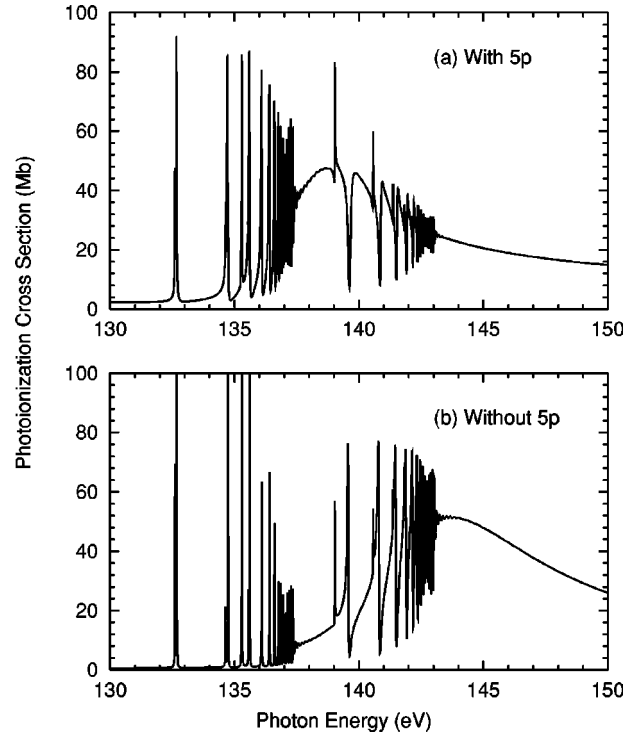


FIG. 5. The $4d$ photoabsorption spectra of Eu^+ ions calculated (a) with $5p$ orbital and (b) without $5p$ orbital.

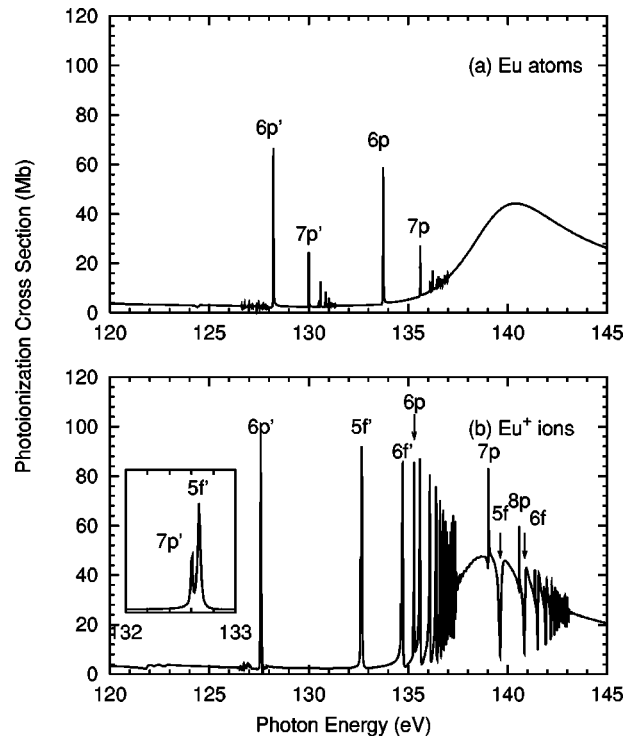


FIG. 6. Spectral assignments of Fig. 1 in the sharp and window resonance region for (a) Eu atoms and (b) Eu^+ ions. Inset is an enlarged part of the transition to $5f'$ for Eu^+ ions.

maximum at $5f'$ or $6f'$, and no $4f'$ observed. This can be understood as that the $4f$ orbital is still pushed into the outer potential well and the $5f'$ or $6f$ orbital collapse into the inner potential well. All the other peaks are assigned as shown in Fig. 6. Since the np' peak position is quite closer to the f' states, we have enlarged the $5f'$ peak in the inset of Fig. 6(b) and found the $7p'$ state next to the $5f'$ with a narrow width. The $8p'$ state is quite close to the $6f'$ peak and so on.

Since our calculation is based on a nonrelativistic local spin-density functional theory, to compare with the experiment, we have to consider the spin-orbital splitting as we did in the Xe-like isoelectronic sequence. Meanwhile the spin-up and spin-down is not a good quantum number even in the nonrelativistic theory. We know that the $4d$ electron of Eu atoms has two ionization limits, 9D and 7D . As a matter of fact, the photoionization of $4d$ spin-down electron of Eu atoms corresponds to 9D channel and $4d$ spin-up electron corresponds to the mixture of the 9D and 7D channels (spin

contamination). We cannot decompose them in the linear-density-response calculation. But the general feature, namely, the sharp and window resonances in our predictions, should still hold.

IV. SUMMARY

The $4d$ photoabsorption process of Eu^+ ions has been studied by the linear-density-response theory with the density-functional theory and optimized effective-potential method. The discrepancies between the calculated and the experiment spectra are well explained being due to the experimental energy resolution. The mechanisms of the sharp resonance as well as the window resonance have been also explained by decomposing individual orbital contributions. The resonance peaks in the calculated spectra are assigned. The calculated spectrum of Eu^+ ions call for a further higher-resolution experiment, which will be performed in the near future [21].

-
- [1] T. Hayaishi, Y. Morioka, Y. Kageyama, M. Watanabe, I.H. Suzuki, A. Mikuni, G. Isoyama, S. Asaoka, and M. Nakamura, *J. Phys. B* **17**, 3511 (1984).
 - [2] J. P. Connerade, J. E. Esteve, and R. C. Karnatak, *Giant Resonance in Atoms, Molecules, and Solids* (Plenum, New York, 1986).
 - [3] M.Y. Amusya, K.V. Ivanov, and V.A. Kupchenko, *Z. Phys. D: At., Mol. Clusters* **14**, 219 (1989).
 - [4] K.T. Cheng and W.R. Johnson, *Phys. Rev. A* **28**, 2820 (1983).
 - [5] K.T. Cheng and C.F. Fischer, *Phys. Rev. A* **28**, 2811 (1983).
 - [6] X.M. Tong, J.M. Li, and R.H. Pratt, *Phys. Rev. A* **42**, 5348 (1990).
 - [7] X.M. Tong, *Acta Phys. Sin.* **40**, 693 (1991).
 - [8] T. Nagata, M. Yoshino, T. Hayaishi, Y. Itikawa, Y. Itoh, T. Koizumi, T. Matsuo, Y. Sato, E. Shigemase, Y. Takizawa, and A. Yagishita, *Phys. Scr.* **41**, 47 (1990).
 - [9] G. Kutluk, Doctoral thesis, Meisei University, 1993.
 - [10] T.M. Kojima, M. Oura, N. Watanabe, Y. Awaya, Y. Itoh, T. Koizumi, M. Sano, and F. Koike, *J. Phys. B* **31**, 1463 (1998).
 - [11] U. Fano and J.W. Cooper, *Phys. Rev.* **137**, A1364 (1965).
 - [12] X.M. Tong, D. Kato, T. Watanabe, and S. Ohtani, *J. Phys. B* **33**, 717 (2000).
 - [13] A. Zangwill and P. Soven, *Phys. Rev. A* **21**, 1561 (1980).
 - [14] E. Runge and E.K.U. Gross, *Phys. Rev. Lett.* **52**, 997 (1984).
 - [15] E.K.U. Gross and W. Kohn, *Phys. Rev. Lett.* **55**, 2850 (1985).
 - [16] G. D. Mahan and K. R. Subbaswamy, *Local Density Theory of Polarizability* (Plenum Press, New York, 1990).
 - [17] M. Stener, P. Decleva, and A. Lisini, *J. Phys. B* **28**, 4973 (1995).
 - [18] A. Fetter and J. Walecka, *Quantum Theory of Many-Body Systems* (McGraw-Hill, New York, 1971).
 - [19] X.M. Tong and S.I. Chu, *Phys. Rev. A* **55**, 3406 (1997).
 - [20] J. Chen, J. Krieger, Y. Li, and G. Iafate, *Phys. Rev. A* **54**, 3939 (1996).
 - [21] T. M. Kojima (private communication).